Title

Spectroscopic fingerprint of chiral Majorana modes at the edge of a quantum anomalous Hall insulator/superconductor heterostructure

Journal

Proceedings of the National Academy of Sciences of the United States of America, 117(1)

ISSN

0027-8424

Authors

Shen, Junying
Lyu, Jian
Gao, Jason Z
et al.

Publication Date

2020-01-07

DOI

10.1073/pnas.1910967117

Peer reviewed

Spectroscopic fingerprint of chiral Majorana modes at the edge of a quantum anomalous Hall insulator/superconductor heterostructure

Junying Shen[a], Jian Lyu[a,b], Jason Z. Gao[a], Ying-Ming Xie[a], Chui-Zhen Chen[a], Chang-woo Cho[a], Omargeldi Atanov[a], Zhijie Chen[c,d], Kai Liu[c,d], Yajian J. Hu[e], King Yau Yip[e], Swee K. Goh[e], Qing Lin He[f,g], Lei Pan[f,h,i], Kang L. Wang[f,h,i,1], Kam Tuen Law[a,1], and Rolf Lortz[a,1]

[a]Department of Physics, The Hong Kong University of Science and Technology, Kowloon, Hong Kong; [b]Department of Physics, Southern University of Science and Technology, 518055 Shenzhen, China; [c]Physics Department, University of California, Davis, CA 95616; [d]Physics Department, Georgetown University, Washington, DC 20057; [e]Department of Physics, The Chinese University of Hong Kong, Shatin, Hong Kong; [f]Department of Electrical and Computer Engineering, University of California, Los Angeles, CA 90095; [g]International Center for Quantum Materials, School of Physics, Peking University, 100871 Beijing, China; [h]Department of Physics, University of California, Los Angeles, CA 90095; and [i]Department of Materials Science and Engineering, University of California, Los Angeles, CA 90095

Edited by Angel Rubio, Max Planck Institute for the Structure and Dynamics of Matter, Hamburg, Germany, and approved November 21, 2019 (received for review June 26, 2019)

With the recent discovery of the quantum anomalous Hall insulator (QAHI), which exhibits the conductive quantum Hall edge states without external magnetic field, it becomes possible to create a topological superconductor (SC) by introducing superconductivity into these edge states. In this case, 2 distinct topological superconducting phases with 1 or 2 chiral Majorana edge modes were theoretically predicted, characterized by Chern numbers ($\mathcal{N}$) of 1 and 2, respectively. We present spectroscopic evidence from Andreev reflection experiments for the presence of chiral Majorana modes in an Nb/$(Cr_{0.12}Bi_{0.26}Sb_{0.62})_2Te_3$ heterostructure with distinct signatures attributed to 2 different topological superconducting phases. The results are in qualitatively good agreement with the theoretical predictions.

topological superconductivity | Majorana fermion | Andreev reflection

Topological superconductors (SCs) which host Majorana zero-energy modes (1) have attracted great interest (2–5), since they represent ideal candidates for fault-tolerant qubits with nonabelian exchange statistics (6–8). One way to realize Majorana states motivated by a model proposed by Kitaev (9) is based on semiconductor nanowires with strong Rashba spin–orbit coupling in which superconductivity is induced by the proximity to an S-wave SC (10–12). This forms topological superconductivity of class D, which breaks the time reversal symmetry. Majorana zero modes at each end of the wire were identified recently by the characteristic quantized zero-bias conductance peak in their tunneling characteristics (13, 14). An alternative system is the chiral P-wave SC, which has been reported to occur intrinsically in Sr_2RuO_4 (15) and predicted to occur when a quantum anomalous Hall insulator (QAHI) with chiral edge modes is made superconducting via the proximity effect (16–19). A topological SC of D class is then expected, which has 2 distinct topological superconducting phases with either 2 or 1 chiral Majorana edge states. In the QAHI, dissipationless conductive chiral quantum Hall edge states classified by a Chern number $C = \pm 1$ are generated by introducing perpendicular ferromagnetism into topological insulator (TI) films by doping with magnetic ions (20, 21). During a magnetization reversal, an additional topologically trivial insulating phase was observed (22, 23). When superconductivity is induced into these chiral edge channels, a topological superconducting phase is expected, which is classified by another Chern number $\mathcal{N} = \pm 2$. The chiral QAHI edge state then consists of 2 degenerated chiral Majorana states (16–19). When approaching the trivial insulating phase, one of the Majorana modes diffuses into the bulk and annihilates, forming an intermediate phase $\mathcal{N} = \pm 1$ with only one chiral Majorana state as a distinct topological superconducting phase (16–19). These chiral Majorana edge states would be excellent candidates for the realization of scalable topological quantum computation by constructing networks of quasi-one-dimensional QAHI/SC structures (24). In ref. 25 a device was presented in which a superconducting strip was deposited on a QAHI. Quantized half-integer conductance plateaus with a value of $0.5e^2/h$ were reported and interpreted as a consequence of the $\mathcal{N} = \pm 1$ phase (26, 27). However, these results provoked various controversies, and it was theoretically argued (28, 29) and experimentally demonstrated (30) that such plateaus could occur under certain circumstances without superconductivity.

In this article, we present an alternative approach based on Andreev reflection experiments using nanoscale point contacts at the edge of a QAHI/SC heterostructure, to investigate the low-energy excitations during the topological transitions. We find a dip-like structure surrounded by 2 peaks, which agrees with the theoretical prediction of the state $\mathcal{N} = \pm 2$ (19), in which the resonant Andreev reflection signals of the 2 Majorana modes

Significance

With the recent involvement of large companies in the development of quantum computation, we are at a stage where this technology appears to be being realized. However, we also urgently need new materials to engineer qubits that are more immune to quantum decoherence processes and can easily be entangled. Majorana fermion in the form of condensed matter quasiparticles is considered the key to a topological qubit that would be much more robust against decoherence. One way to develop such a qubit is to introduce superconductivity into a quantum anomalous Hall insulator. We provide spectroscopic evidence of chiral Majorana modes in this material in qualitatively good agreement with the theoretical predictions.

Author contributions: K.T.L. and R.L. designed research; J.S., J.L., J.Z.G., Y.-M.X., C.-Z.C., C.-w.C., O.A., Y.J.H., K.Y.Y., S.K.G., K.T.L., and R.L. performed research; J.Z.G., Y.-M.X., and C.-Z.C. performed numerical simulations; Z.C., K.L., Q.L.H., L.P., and K.L.W. contributed new reagents/analytic tools; R.L. analyzed data; and R.L. wrote the paper.

The authors declare no competing interest.

This article is a PNAS Direct Submission.

Data deposition: The experimental d*I*/d*V* raw data in this article are available at https://data.4tu.nl/repository/uuid:4e112e65-36ab-4046-bcd5-6f11a7c09d80.

[1]To whom correspondence may be addressed. Email: wang@ee.ucla.edu, phlaw@ust.hk, or lortz@ust.hk.

This article contains supporting information online at https://www.pnas.org/lookup/suppl/doi:10.1073/pnas.1910967117/-/DCSupplemental.

First published December 18, 2019.

cancel each other at small bias voltage (19). As the field is increased and a reversal of magnetization is induced, the dip transforms into a plateau, as expected when the state $\mathcal{N} = \pm 1$ is formed (19). These results suggest the presence of 2 distinct topological superconducting phases.

Results

A sketch of this edge point contact device is shown in Fig. 1*A*. The heterostructure of total area 5 × 2 mm^2 consisted of a 6-nm $(Cr_{0.12}Bi_{0.26}Sb_{0.62})_2Te_3$ film on a GaAs (111) substrate and was entirely covered by a 200-nm Nb layer, with nanopoint contacts in the form of 200- to 500-nm-wide metal strips at the edge of the heterostructure. Our nanopoint contact method is a very local spectroscopic probe and thus is largely unaffected by domain structures (27–29) in the QAHI film. The contacts are so small that edge states of individual domains can be investigated (30). For more details on sample growth and device fabrication, see *Methods*. Fig. 1*B* shows the sharp resistive $T_c = 7.2$ K of Nb, and Fig. 1*C* shows the upper critical field transition in the magnetoresistance at $H_{c2}(273\ \text{mK}) = 9$ T, demonstrating a high quality of the Nb film.

In our nanopoint contact setup, it was inevitable and even essential that a parallel contact with the Nb layer was established, and the measured differential conductance (dI/dV) spectra typically contained contributions from both layers. Different contacts showed different characteristics due to different barrier heights between electrode and Nb or $(Cr_{0.12}Bi_{0.26}Sb_{0.62})_2Te_3$ layers. In Fig. 1*D*, we show a selection of typical raw data of contact 1, which was in the highly transparent Andreev limit (contact resistance < 100 ohm). The dI/dV data are dominated by a broad peak centered at zero bias. The main contribution can be identified as a result of Andreev reflections from the Nb layer, as the fits with the Blonder–Tinkham–Klapwijk (BTK) model (31) show ($Z = 0.01$, $\Delta = 1.6$ meV, $\Gamma = 0.6$ meV), where Z is the effective barrier strength, Δ is the superconducting gap value, and Γ is the finite quasi-particle lifetime or broadening parameter. Note that these parameters are dominated by the contact to Nb, and the parameters for the parallel contact to the QAHI may differ somewhat. For more details on fitting, see *Methods*. Note that, due to the high H_{c2} of Nb, no significant magnetic field dependence is expected for the small field range of interest in our experiments. The Nb contribution in zero field is superimposed by a small feature with 2 symmetric peaks that flatten the tip of the Nb delta shape. To isolate the contribution of proximity-induced superconductivity in the QAHI, we apply a 175-mT magnetic field known to drive the QAHI into the trivial insulating state (22, 23, 25, 32) in which the conducting edge state vanishes, and thus proximity-induced superconductivity is entirely suppressed. At a sufficiently low bias voltage (below ±2 mV), these spectra originate only from the Nb contribution, which were then used to isolate the QAHI contribution in data in lower and higher fields. At higher bias voltages, strong oscillations are seen, which are attributed to bulk electronic bands in the QAHI.

In Fig. 1*E*, we show data from a contact in the low-transparency tunneling limit (contact 2) fabricated on the same heterostructure. Here, the Nb contribution appears as a shallow, broad gap. A fit of this contribution with the BTK model is included ($Z = 8$, $\Delta = 2.3$ meV, $\Gamma = 1.5$ meV), which describes the data well with a gap value of 2.3 meV, which corresponds to the literature data of bulk Nb (33). Two peaks surrounding a dip appear here at lower bias voltage, which transform in a plateau in a field of 100 mT, shortly before the QAHI enters the trivial insulating state. As we will show below, this is the expected signature of chiral Majorana fermions in the QAHI layer. While this contact would be ideal to investigate these features without background subtraction, it unfortunately became unstable, and therefore we will focus on contact 1, which has the same features attributed to a superconducting QAHI edge state after separation of the Nb background. For comparison, we have included the 0T data of contact 1, which, in the region of the proximity gap at low bias voltage, show excellent agreement with the raw data of contact 2. This demonstrates that the 175-mT data represent an ideal background for all data of contact 1, which is justified since no edge conduction occurs in the trivial insulating state and thus the QAHI does not contribute to the point contact spectrum in this field. For chiral Majorana modes, it has been theoretically shown that any form of tunneling from a lead to

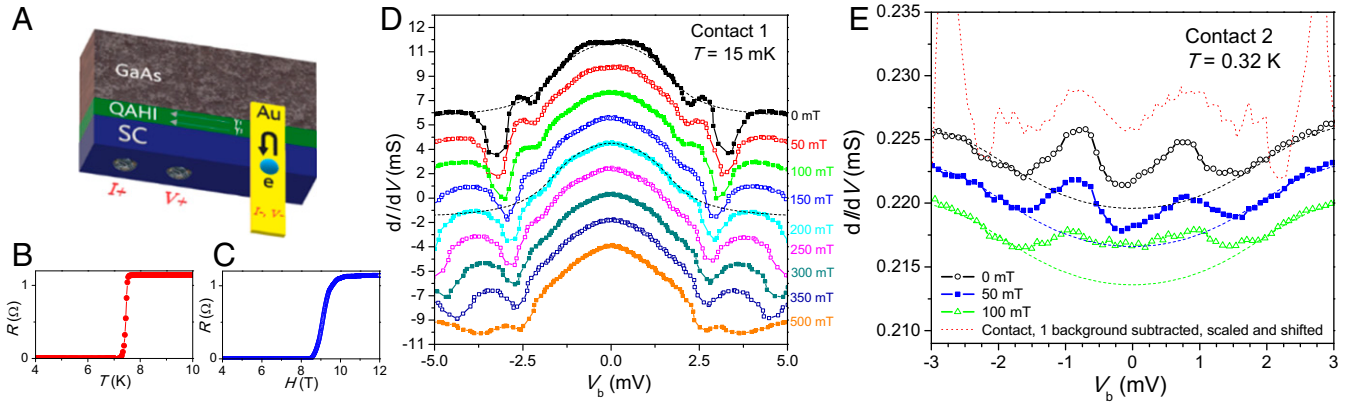

Fig. 1. (*A*) Sketch of the point contact device on the edge of a QAHI/SC heterostructure. It features normal contacts on the surface of a superconducting Nb layer and point contacts realized by thin Au strips crossing the edge of the heterostructure. The arrows illustrate the Andreev reflection process. Note that the dimensions of the sketch are not to scale: The actual film dimensions were 5 mm × 2 mm, while the thickness of the QAHI was 6 nm and the Nb thickness was 200 nm. (*B*) Zero-field electrical resistance measured by 4 ohmic contacts on the surface of the Nb layer. The sharp resistance jump defines $T_c = 7.2$ K. (*C*) Magnetoresistance measured at $T = 273$ mK as a function of a magnetic field applied perpendicular to the film. The jump marks $H_{c2} = 9$ T. (*D*) High-transparency point contact spectroscopy raw data dI/dV of contact 1. A dominant superconducting Nb contribution is seen as a large positive Andreev reflection peak (31). (*E*) Low-transparency point contact spectroscopy data dI/dV of another QAHI/SC heterostructure (contact 2). The Nb contribution shows up as a broad shallow gap. The QAHI contribution can be seen here without any background subtraction (the 50 mT and 100 mT data were shifted by −2.5 and −5.0 μS, respectively). Scaled zero-field data of contact 1 after subtraction of the Nb contribution have been added for comparison. Note that the additional oscillations at higher bias voltage beyond ±2 mV are attributed to the bulk bands of the QAHI. Fits of the SC Nb background with the BTK model (31) have been included in *D* and *E* (dashed lines).

the edge of the superconducting QAHI occurs via resonant Andreev reflection (19). Therefore, although contacts 1 and 2 have completely different transparency, the presence of Majorana modes is expected to manifest in a form of the same shape in dI/dV, while less transparent contacts only reduce the amplitude.

In the following, we investigate, with contact 1, how the contribution to dI/dV from the QAHI changes when the QAHI is driven back and forth through the magnetization reversal, and thus investigate the entire range of magnetization hysteresis to search for signatures of topological transitions in a superconducting QAHI state. In Fig. 2, we show 2 series of differential conductance data from contact 1, after subtraction of the Nb contribution, which were taken during the magnetization reversal of $(Cr_{0.12}Bi_{0.26}Sb_{0.62})_2Te_3$ by repeated measurements upon small 25-mT increments (decrements) of the magnetic field, starting from a negative (positive) field of −500 mT (+500 mT) toward a positive (negative) field of +500 mT (−500 mT). The start field of −500 mT (Fig. 2*A*) or +500 mT (Fig. 2*B*) is used to fully magnetize the QAHI insulator before the experiment. In Fig. 2*A* the field is changed from negative to positive fields, and, in Fig. 2*B*, the field is changed in the opposite direction. Due to the magnetic hysteresis, magnetization is maintained when the field is reduced to zero, and the reversal of magnetization is induced when the field reaches the opposite polarity in the field range between 150 mT (−150 mT) and 200 mT (−200 mT) (22). The data have been shifted vertically by $2e^2/h$ (except for the ±150 mT data) for better visualization. Both datasets show exactly the same trend. At −100 mT (+100 mT), the data show a characteristic dip at zero bias framed by 2 peaks around ±0.75 mV, indicating the presence of proximity-induced superconductivity in the QAHI. As we will show later, we attribute them to the $\mathcal{N}=-2$ ($\mathcal{N}=+2$) topological superconducting states in which the cancellation of Andreev reflection amplitudes of a pair of chiral Majorana modes causes a suppression of the conductance around zero bias (19). The plus or minus signs refer to the direction of the QAHI magnetization. As the magnitude of the applied field is gradually reduced, the size of the dip and peaks increases and reaches a maximum at zero field. After crossing the zero field, the amplitude further decreases until, at +100 mT (−100 mT), the dip changes into a plateau with relatively sharp edges at ±0.7 mV, which we will show later is attributed to the $\mathcal{N}=-1$ ($\mathcal{N}=+1$) topological superconducting states. The plateau persists at +125 mT (−125 mT), while it vanishes at +150 mT (−150 T). By further increasing the field strength to +175 mT (−175 mT) and 200 mT (−200 mT), the data become flat, indicating that the QAHI enters the trivial insulating state in which proximity-induced superconductivity vanishes during the magnetization reversal. Note that the same transition to a plateau can be seen in the raw data of contact 2 in Fig. 1*E* at 100 mT, without the need for background subtraction.

In Fig. 3*A*, we show selected data from the 3 topological regimes without shift to further illustrate the differences in the spectra. In the $\mathcal{N}=1$ state, the plateau-like feature differs significantly from the spectra in the $\mathcal{N}=2$ state with its characteristic dip around zero bias and from the trivial insulating state in which the conductance remains zero. The plateau of the $\mathcal{N}=1$ state clearly differs from the expected signature of a trivial metallic state, in which the plateau would extend to a wide voltage range. Here the $\mathcal{N}=1$ plateau is limited to the bias voltage range associated with the superconducting proximity gap, which is about 0.7 meV, and vanishes abruptly at higher bias voltage. It is also important to note that the drop in dI/dV forming the edge of the plateau at 0.7 meV is unlikely to be caused by the superconducting Nb background, since the pairing gap of Nb is estimated to be at least 1.6 meV in our experiment. Furthermore, the height for this contact remains close to the conductance quantum $2e^2/h$. We would also like to point out that, at both contact 1 and contact 2, a plateau of the same shape is observed, although the height of the tunneling barrier differs strongly. This can be plausibly explained by resonant Andreev reflection processes in the presence of Majorana modes (19), whereas the spectra of ordinary SCs would look completely different in the 2 regimes (31).

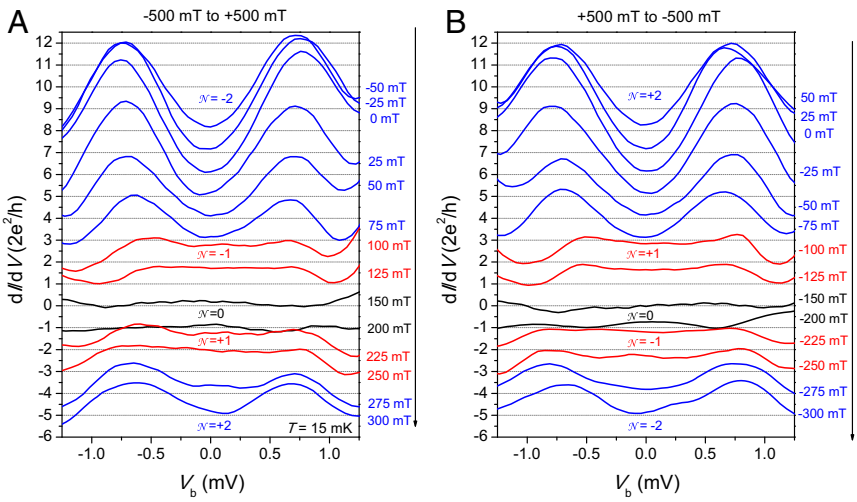

Fig. 2. Differential conductance of a point contact at the edge of the $(Cr_{0.12}Bi_{0.26}Sb_{0.62})_2Te_3$/Nb heterostructure at 15 mK (contact 1), after the subtraction of the Nb contribution. The data in *A* were taken starting from a negative field upon increasing the field in 25-mT increments to positive fields, inducing the QAHI's magnetization reversal at ∼175 mT, while, for the data in *B*, the opposite direction of field change was used to study the entire hysteresis range of magnetization. Dips surrounded by 2 peaks mark the $\mathcal{N}=\pm2$ topological superconducting regions, while flat plateaus are observed at (*A*) +100 mT and +125 mT or (*B*) −100 mT and −125 mT, which are attributed to the $\mathcal{N}=\pm1$ topological superconducting phases. The latter occurs shortly before the QAHI enters the trivial insulating region ($\mathcal{N}=0$). When the absolute value of the magnetic field increases further, a reentry of the $\mathcal{N}=\pm1$ phase in the form of the plateau at 225 mT (−225 mT) is seen, and, finally, the characteristic dip of the $\mathcal{N}=\pm2$ phase occurs again. These features are unique to $(Cr_{0.12}Bi_{0.26}Sb_{0.62})_2Te_3$ in proximity to the superconducting Nb layer and occur within the insulating bulk gap region of $(Cr_{0.12}Bi_{0.26}Sb_{0.62})_2Te_3$. Offsets of $2e^2/h$ have been added for better clarity, except for the ±150 mT data.

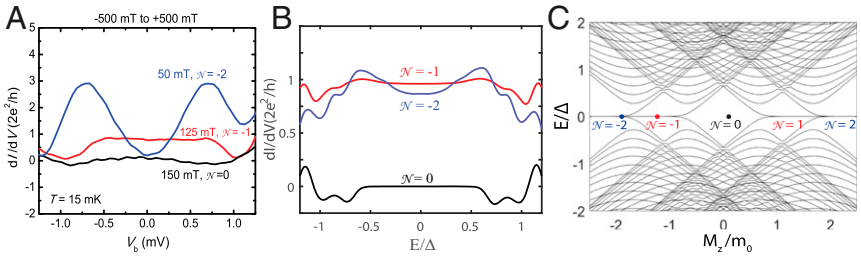

Fig. 3. (*A*) Selected data of the differential conductance of contact 1 ($T = 15$ mK) without offsets, to illustrate the difference of the spectra in the different topological regimes. (*B*) Simulated d*I*/d*V* as a function of the bias voltage energy (normalized by the SC energy gap Δ) for selected magnetization energy values of $M_z = 0.01\ m_0$ ($\mathcal{N} = 0$), $-1.2m_0$ ($\mathcal{N} = -1$), $-1.85m_0$ ($\mathcal{N} = -2$). Dips at zero bias mark the chiral fermionic modes in the $\mathcal{N} = \pm 2$ topological superconducting region, while a flat plateau indicates the single chiral Majorana mode in the $\mathcal{N} = \pm 1$ topological superconducting phase. In contrast, the trivial insulating state with $\mathcal{N} = 0$ shows a vanishing conductance in a range around the zero bias voltage. The details of the simulations can be found in *SI Appendix*. (*C*) Energy spectrum at the Γ point as a function of M_z. The 5 topologically distinct regions are separated by points at which the bulk energy gap closes. The image shows a series of phase transitions from the $\mathcal{N} = -2$ to the $\mathcal{N} = +2$ topological SC as a function of M_z (m_0 is the intrinsic magnetization energy). The 3 solid dots on the central horizontal axis represent the 3 M_z values of the data in *B*.

Upon further increasing (decreasing) the applied field in 25-mT steps, the QAHI continuous to evolve from the trivial insulating state toward the fully magnetized $C = +1$ state. At 225 mT (−225 mT), a flat plateau associated with the $\mathcal{N} = +1$ ($\mathcal{N} = -1$) phase reappears. When sweeping the field further, at +275 mT (−275 mT), the plateau changes back into 2 peak-like structures surrounding a dip around zero bias. This indicates a reentry of the topological state with 2 chiral Majorana modes ($\mathcal{N} = +2$). We would like to point out once again that the main features, namely the transition from a peak–dip-like feature ($\mathcal{N} = 2$) to a plateau-like feature ($\mathcal{N} = 1$) is also visible in the raw data of contact 2 without the need to subtract background data, which gives us a high degree of confidence in these results.

Further data of contact 1 are included in *SI Appendix*. It shows selected data recorded during an additional field cycle and data at a higher temperature of 280 mK, thus demonstrating the reproducibility of the results. We also show similar data from another heterostructure grown under identical transition (contacts 3 and 4). For our contacts in the high-transparency Andreev limit (contacts 1 and 3), the plateau associated with the $\mathcal{N} = \pm 1$ state appears to be not far from quantization at a conductance of $\sim 2e^2/h$.

Discussion

In the following, we will show that the transition from a dip-like feature at zero bias to a conductance plateau as a function of magnetic field is indeed expected when the QAHI changes from the $\mathcal{N} = +2$ state with 2 chiral Majorana edge modes to the $\mathcal{N} = +1$ state in which only 1 chiral Majorana mode remains at the edge (18, 19). The magnetic TI thin film $(Cr_{0.12}Bi_{0.26}Sb_{0.62})_2Te_3$ can be described by $\mathcal{H}_{TI} = \Sigma_k \Psi_k{}^\dagger H_{TI} \Psi_k$ in the basis of $\Psi_k = [\psi_{t\uparrow}, \psi_{t\downarrow}, \psi_{b\uparrow}, \psi_{b\downarrow}]^T$, where ψ denotes an electron annihilation operator (26). Explicitly,

$$H_{TI}(k) = \begin{pmatrix} h_t(\boldsymbol{k}) & m_{\boldsymbol{k}} \\ m_{\boldsymbol{k}} & h_b(\boldsymbol{k}) \end{pmatrix},$$

with $h_{t,b}(k) = \pm v_F(k_y\sigma_x - k_x\sigma_y) + M_z\sigma_z$. Here the Pauli matrices $\sigma_{x,y,z}$ act on spin (↑/↓) space, *t*/*b* denotes the top/bottom surface of the TI thin film, and $m_{\boldsymbol{k}} = m_0 + m_1k^2$ describes the hybridization between the 2 surfaces, while v_F is the Fermi velocity of the surface Dirac fermions. The magnetization energy, M_z, is caused by intrinsic magnetic dopants as well as an external magnetic field. The magnetic TI thin-film Hamiltonian is in $C = M_z/|M_z|$ QAHI phase with a chiral fermionic edge mode at the boundary when $|M_z| > |m_0|$, while becoming a $C = 0$ normal insulator when $|M_z| < |m_0|$.

In proximity to an *S*-wave SC, the effective Hamiltonian of the $(Cr_{0.12}Bi_{0.26}Sb_{0.62})_2Te_3$/SC heterostructure in the Bogoliubov–de Gennes (BdG) space becomes

$$\mathcal{H}_{BdG} = \begin{pmatrix} H_{TI}(\boldsymbol{k}) - \mu & \Delta_{\boldsymbol{k}} \\ \Delta_{\boldsymbol{k}}{}^\dagger & -H^*{}_{TI}(-\boldsymbol{k}) + \mu \end{pmatrix},$$

where

$$\Delta_{\boldsymbol{k}} = \begin{pmatrix} \Delta_t i\sigma_y & 0 \\ 0 & \Delta_b i\sigma_y \end{pmatrix}.$$

Here, μ is the chemical potential, and $\Delta_{\boldsymbol{k}}$ denotes the induced *S*-wave pairing with $\Delta_t = \Delta$ and $\Delta_b = 0$. In general, the $\mathcal{N} = \pm 2$ superconducting phase is topologically equivalent to the $C = \pm 1$ QAHI phase; that is, a single chiral fermion edge state can be regarded as 2 branches of chiral Majorana edge states. The $\mathcal{N} = \pm 1$ phase is a new topological phase that supports one single Majorana fermion that propagates along the edges of the sample (16–19). Further details about the Green's Function formalism used for the calculations of the tunneling conductance based on $\mathcal{H}_{BdG}$ can be found in ref. 19 and in *SI Appendix*.

Fig. 3*C* shows the energy spectrum at the Γ point of the topological SC, that is, the proximity coupled QAHI strip with the pairing gap interaction, as a function of M_z, normalized by the intrinsic magnetization energy m_0. The topological invariant $\mathcal{N}$ can only change at the points where the bulk gap closes (16). This defines 5 topologically distinct regions separated by 4 gap closure points. In the following, we will show that the topological regions with 1 ($\mathcal{N} = \pm 1$) or 2 ($\mathcal{N} = \pm 2$) pairs of Majorana edge modes have very different transport properties. A selection of simulated tunneling conductance $dI/dV = (2e^2/h)Tr(R_{he}R_{he}{}^\dagger)$ (19) for different magnetization energy values of M_z from a metal lead to the edge of a QAHI/SC heterostructure has been included in Fig. 3*B* for qualitative comparison with the experimental data in Fig. 3*A*. Here R_{he} stands for the local Andreev reflection amplitude. In the experiment, M_z is controlled by the applied magnetic field. The M_z values of the 3 conductance plots in Fig. 3*B* are indicated on the horizontal axis of the energy spectrum plot in Fig. 3*C*. To compare with the experimental data in Fig. 3*A*, the 3 conductance plots in Fig. 3*B* are obtained by subtracting the conductance of the $\mathcal{N} = 0$ state with $M_z = 0$ from the data as background. Since the $\mathcal{N} = 0$ state with $M_z = 0$ has a zero conductance for energy smaller than the pairing gap, this subtraction has no influence on the in-gap conductance for the $\mathcal{N} = -1$ and $\mathcal{N} = -2$ states. From Fig. 3*B*, we can clearly see the conductance dip in the $\mathcal{N} = -2$ state and the conductance plateau in the $\mathcal{N} = -1$ state, as

predicted in ref. 19 and observed in the experiment. Further details on the conductance plots, including the data without subtraction of the background conductance, are contained in *SI Appendix*.

While the experimental conductance of the $\mathcal{N}=\pm1$ plateau suggests a quantization near $2e^2/h$, the simulations show that the absolute height varies slightly with subtle parameter changes (e.g., the tunneling barrier height; see *SI Appendix*, section 5 for a more detailed discussion). Precise quantization is only expected for metallic leads coupled to a single Majorana zero mode, but not for leads coupled to dispersive chiral Majorana edge modes. The value of the height of the $\mathcal{N}=\pm1$ plateau of $2e^2/h$ is therefore likely a coincidence.

Methods

The QAHI films $(Cr_{0.12}Bi_{0.26}Sb_{0.62})_2Te_3$ (6-nm thickness) were grown on GaAs (111) substrates in an ultrahigh vacuum molecular beam epitaxy system at University of California, Los Angeles. The Nb layer (200-nm thickness) was sputtered onto the QAHI layer, which, for technical reasons, was done at University of California, Davis. Note that this is different from other approaches (32), where the Nb layer was deposited in the same vacuum chamber, and may result in differences in coupling between the 2 materials. All experiments were conducted by the group of the Hong Kong University of Science and Technology.

Slabs of ~2 mm × 5 mm were cut from the wafer, and the long edge of the heterostructure was finely polished, before layers of Ti (5 nm) and Au (80 nm) were deposited. A focused ion beam was used to define small isolated metal strips with width (W) of a few hundred nanometers that traverse the entire substrate and film edge. These edge contacts (area: $W \times 206$ nm) represent small nanopoint contacts of a few tens of ohms up to several kiloohms of resistance at ambient temperature and thus enable point contact measurements from the highly transparent Andreev regime to the low-transparent tunneling regime (31). It should be noted that a certain roughness of the edge was desired to prevent the superconducting signal from Nb being too dominant. This is the reason for a quite broad gap signature of the Nb signal. Differential conductance vs. bias voltage measurements were conducted in a dilution refrigerator with the magnetic field strictly perpendicular to the film. Data from 3 devices are included in this article: Contact 1 and contact 2 were fabricated on the same heterostructure, while contact 3 was fabricated on another heterostructure grown under identical conditions.

We used fits with the BTK model to identify the superconducting contribution of Nb in a 175-mT field where the QAHI is in the trivial insulating state. The BTK theory analyzes the differential conductance vs. bias voltage with the superconducting order parameter Δ and barrier height Z as fitting parameters. We used a modified BTK model that takes into account the finite quasi-particle lifetime or broadening parameter Γ (34). More details can be found in *SI Appendix*, section 7.

Data Availability. The experimental d*I*/d*V* raw data in this article are available at https://data.4tu.nl/repository/uuid:4e112e65-36ab-4046-bcd5-6f11a7c09d80.

ACKNOWLEDGMENTS. R.L. acknowledges enlightening discussions with X.-G. Wen, H. Zhang, M. He, and X. Dai; and support by grants from the Research Grants Council of the Hong Kong Special Administrative Region, China (HKRGC) (Grants GRF-16302018, SBI17SC14, and IEG16SC03). K.T.L. acknowledges the support of HKRGC through Grant C6026-16W, the Croucher Foundation, and the Tai-chin Lo Foundation. S.K.G. acknowledges the support from the HKRGC Grant GRF-14300418. K.L.W. and Q.L.H. acknowledge the support of the Army Research Office Multiple University Research Initiative and Energy Frontier Research Center. Q.L.H. also acknowledges support from the National Natural Science Foundation of China (Grant 11874070), the National Key R&D Program of China (Grant 338 2018YFA0305601), and the National Thousand-Young Talents Program in China. Z.C. and K.L. acknowledge support from the US NSF (Grants DMR-1610060 and DMR-1905468).

1. E. Majorana, Teoria simmetrica dell'elettrone e del positrone. *Nuovo Cim.* **14**, 171–184 (1937).
2. M. Sato, Y. Ando, Topological superconductors: A review. *Rep. Prog. Phys.* **80**, 076501 (2017).
3. X.-L. Qi, S.-C. Zhang, Topological insulators and superconductors. *Rev. Mod. Phys.* **83**, 1057–1110 (2011).
4. C. W. J. Beenakker, Search for Majorana fermions in superconductors. *Annu. Rev. Condens. Matter Phys.* **4**, 113–136 (2013).
5. J. Alicea, New directions in the pursuit of Majorana fermions in solid state systems. *Rep. Prog. Phys.* **75**, 076501 (2012).
6. F. Wilczek, Majorana returns. *Nat. Phys.* **5**, 614–618 (2009).
7. S. D. Sarma, M. Freedman, C. Nayak, Majorana zero modes and topological quantum computation. *npj Quantum Inf.* **1**, 15001 (2015).
8. C. Nayak, S. H. Simon, A. Stern, M. Freedman, S. D. Sarma, Non-abelian anyons and topological quantum computation. *Rev. Mod. Phys.* **80**, 1083–1159 (2008).
9. A. Y. Kitaev, Unpaired Majorana fermions in quantum wires. *Phys. Uspekhi* **44**, 131–136 (2001).
10. J. Alicea, Majorana fermions in a tunable semiconductor device. *Phys. Rev. B* **81**, 125318 (2010).
11. Y. Oreg, G. Refael, F. von Oppen, Helical liquids and Majorana bound states in quantum wires. *Phys. Rev. Lett.* **105**, 177002 (2010).
12. P. W. Brouwer, M. Duckheim, A. F. Romito, F. von Oppen, Topological superconducting phases in disordered quantum wires with strong spin-orbit coupling. *Phys. Rev. B* **84**, 144526 (2011).
13. V. Mourik *et al.*, Signatures of Majorana fermions in hybrid superconductor-semiconductor nanowire devices. *Science* **336**, 1003–1007 (2012).
14. H. Zhang *et al.*, Quantized Majorana conductance. *Nature* **556**, 74–79 (2018).
15. S. Kashiwaya *et al.*, Edge states of Sr_2RuO_4 detected by in-plane tunneling spectroscopy. *Phys. Rev. Lett.* **107**, 077003 (2011).
16. X.-L. Qi, T. L. Hughes, S.-C. Zhang, Chiral topological superconductor from the quantum Hall state. *Phys. Rev. B* **82**, 184516 (2010).
17. A. Ii, K. Yada, M. Sato, Y. Tanaka, Theory of edge states in a quantum anomalous Hall insulator/spin-singlet s-wave superconductor hybrid system. *Phys. Rev. B* **83**, 224524 (2011).
18. A. Ii, A. Yamakage, K. Yada, M. Sato, Y. Tanaka, Theory of tunneling spectroscopy for chiral topological superconductors. *Phys. Rev. B* **86**, 174512 (2012).
19. J. J. He *et al.*, Correlated spin currents generated by resonant-crossed Andreev reflections in topological superconductors. *Nat. Commun.* **5**, 3232 (2014).
20. C.-Z. Chang *et al.*, Experimental observation of the quantum anomalous Hall effect in a magnetic topological insulator. *Science* **340**, 167–170 (2013).
21. X. Kou *et al.*, Scale-invariant quantum anomalous Hall effect in magnetic topological insulators beyond the two-dimensional limit. *Phys. Rev. Lett.* **113**, 137201 (2014).
22. X. Kou *et al.*, Metal-to-insulator switching in quantum anomalous Hall states. *Nat. Commun.* **6**, 8474 (2015).
23. Y. Feng *et al.*, Observation of the zero Hall plateau in a quantum anomalous Hall insulator. *Phys. Rev. Lett.* **115**, 126801 (2015).
24. C.-Z. Chen, Y.-M. Xie, J. Liu, P. A. Lee, K. T. Law, Quasi-one-dimensional quantum anomalous Hall systems as new platforms for scalable topological quantum computation. *Phys. Rev. B* **97**, 104504 (2018).
25. Q. L. He *et al.*, Chiral Majorana fermion modes in a quantum anomalous Hall insulator-superconductor structure. *Science* **357**, 294–299 (2017).
26. J. Wang, Q. Zhou, B. Lian, S.-C. Zhang, Chiral topological superconductor and half-integer conductance plateau from quantum anomalous Hall plateau transition. *Phys. Rev. B* **92**, 064520 (2015).
27. C. Z. Chen, J. J. He, D. X. Xu, K. T. Law, Effects of domain walls in quantum anomalous Hall insulator/superconductor heterostructures. *Phys. Rev. B* **96**, 041118 (2017).
28. W. Ji, X.-G. Wen, A mechanism of 1/2e^2/h conductance plateau without 1D chiral Majorana fermions. *Phys. Rev. Lett.* **120**, 107002 (2018).
29. Y. Huang, F. Setiawan, J. D. Sau, Disorder-induced half-integer quantized conductance plateau in quantum anomalous Hall insulator-superconductor structures. *Phys. Rev. B* **97**, 100501 (2018).
30. K. Yasuda *et al.*, Quantized chiral edge conduction on domain walls of a magnetic topological insulator. *Science* **358**, 1311–1314 (2017).
31. G. E. Blonder, M. Tinkham, T. M. Klapwijk, Transition from metallic to tunneling regimes in superconducting microconstrictions: Excess current, charge imbalance, and supercurrent conversion. *Phys. Rev. B* **25**, 4515 (1982).
32. M. Kayyalha *et al.*, Non-Majorana origin of the half-quantized conductance plateau in quantum anomalous Hall insulator and superconductor hybrid structures. arXiv: 1904.06463 (13 April 2019).
33. D. Bonnet, S. Erlenkamper, H. Germer, H. Rabenhorst, A measurement of the energy gap in superconducting niobium. *Phys. Lett. A* **25**, 452–453 (1967).
34. Yu. G. Naidyuk, K. Gloos, Anatomy of point-contact Andreev reflection spectroscopy from the experimental point of view. *Low Temp. Phys.* **44**, 257–268 (2018).